ARTICLE

Improved Catalytic Capability of Mesoporous TiO_2 Microspheres and Photodecomposition of Toluene

Yinchang Feng,[†] Lei Li,[†] Ming Ge,[‡] Changsheng Guo,[‡] Junfeng Wang,*[,‡] and Lu Liu*[,‡]

State Environmental Protection Key Laboratory of Urban Ambient Air Particulate Matter Pollution Prevention and Control and Tianjin Key Laboratory of Environmental Remediation and Pollution Control, Nankai University, Tianjin 300071, People's Republic of China

ABSTRACT A series of mesoporous titanium dioxide microspheres were calcined at various temperatures to improve their photocatalytic activity. The prepared catalysts were characterized by XRD, SEM, TEM, TG-DTA, UV−vis, and N_2 adsorption−desorption measurements, and their photocatalytic performances were investigated by photooxidation of gaseous toluene. As the results revealed, calcination temperatures obviously influenced the surface morphology and photocatalytic activity of the mesoporous TiO_2 microspheres. The noncalcined samples had a mesoporous structure of the anatase phase. The sample calcined at 400 °C showed a superior photocatalytic performance, which had a reaction rate constant 2-fold higher than that of P_{25}. The enhanced photoreactivity is possibly due to the synergetic effects of the mesoporous structure and light-transmittance ability of the catalysts. Two new reaction intermediates were discovered as well, and a tentative degradation pathway was proposed.

KEYWORDS: mesoporous adjustment • titanium dioxide microspheres • photocatalysis • reaction intermediates • mechanism

1. INTRODUCTION

Indoor air pollution represents a serious environmental problem because many people suffer from pollutants from construction projects, interior decorations, and daily necessities. The Environmental Protection Agency of the United States has found that the concentrations of organic matters in indoor air are 2−5 times greater than that in outdoor environments (1). Concentrations of indoor pollutants have been increasing because the turnover rate of indoor air to reduce thermal energy losses in modern airtight buildings is low (2, 3). Research on volatile organic compound (VOC) removal from indoor air has been attracting much interest. Traditional treatment techniques, such as absorption, adsorption, condensation, biofiltration, and catalytic destruction processes, are restricted in application because of several inherent drawbacks or limitations, such as the high cost of equipment and operations, secondary pollution, requirements for advanced treatments (4), etc.

Photocatalytic oxidation (PCO) is a cost-effective and environmentally friendly technology for VOC removal and generally uses semiconductors together with an ultraviolet (UV) or a near-UV light source to convert organic compounds into benign and odorless constituents (H_2O and CO_2) under mild conditions (5−7). However, complex molecules are difficult to degrade, and undesirable intermediates or byproducts can be formed, which sometimes results in photocatalyst deactivation (8). Therefore, the development of a highly reactive photocatalyst for the removal of indoor air pollutants is desirable. A good photocatalyst depends strongly on the efficiency of electron−hole pair separation and the adsorption ability of organic substrates on the surface of the catalyst (9, 10). Among various semiconductor photocatalysts, TiO_2-related materials have been proven to be the most efficient catalysts for widespread environmental applications because of their high quantum yields, biological and chemical inertness, low cost, nontoxicity, wide availability, strong oxidizing power, and potential for degradation of a broad range of pollutants (especially in the anatase phase or anatase−rutile combinations) (6, 11−14).

Many efforts have been concentrated on the photocatalytic applications of mesoporous nanocrystalline titania for their high surface areas, pore volumes, and uniform pore size distributions, which can supply more active sites for adsorption and photocatalytic reactions. For example, TiO_2 nanorods/nanoparticles with mesoporous structure were synthesized by the hydrothermal method and measured by PCO of a potassium iodide aqueous solution (15, 16). Mesoporous titanium dioxide nanocrystalline powders prepared by the ultrasonic method had provided excellent activity for photooxidation of formaldehyde and acetone mixtures in the gas phase at room temperature (11). Florence and co-workers reported the preparation of mesoporous anatase TiO_2 materials and explained their high toluene removal efficiency by the hypothesis of the inner partial pressure concept instead of a high surface area (14).

The photooxidation of toluene is a very stringent test for the performance of a photocatalyst (13), and toluene is

* To whom correspondence should be addressed. E-mail: jfwangnk@yahoo.com.cn (J.W.), liul@nankai.edu.cn (L.L.).
Received for review July 15, 2010 and accepted October 12, 2010
[†] State Environmental Protection Key Laboratory of Urban Ambient Air Particulate Matter Pollution Prevention and Control.
[‡] Tianjin Key Laboratory of Environmental Remediation and Pollution Control.
DOI: 10.1021/am100620f

Published on Web 10/22/2010

selected as a model pollutant in this paper. The current study was to seek a more active photocatalyst for wide application in indoor air purification. Mesoporous TiO_2 microspheres were synthesized under different calcination temperatures, and their photocatalytic properties on toluene degradation were compared. The objectives of the present study are to determine the effectiveness of photocatalytic degradation of toluene using mesoporous TiO_2 microspheres, identify intermediates of degradation, and determine the mechanisms of the degradation process.

2. EXPERIMENTS

2.1. Preparation of the Materials. All chemicals used in this study were of analytical grade or higher. In a typical procedure, an appropriate amount of NaOH was completely dissolved in 40 mL of absolute ethanol, and then 2 mL of $TiCl_3$ was added dropwise to the solution with vigorous stirring. The resultant transparent solution was put into a 50 mL Teflon-lined autoclave vessel and maintained at 150 °C for 24 h. After the autoclave was naturally cooled, the samples were centrifuged and rinsed thoroughly with distilled water and ethanol several times. After the products were dried at 40 °C for 5 h, they were calcined for 2 h at temperatures from 100 to 800 °C with 100 °C intervals. Different calcination temperatures produced catalysts with different characteristics. In this study, the synthesized TiO_2 microspheres were designated as Ti*x*, where *x* indicated the selected calcination temperature in the range of 100−800 °C.

2.2. Characterization. The phase structure of TiO_2 was evaluated by X-ray diffraction (XRD) on a Rigaku D/Max-2500 diffractometer. Their morphology and sizes were characterized by scanning electron microscopy (SEM; Shimadzu SS-550), field-emission scanning electron microscopy (FESEM; FEI nanosem 430), transmission electron microscopy (TEM; JEM-100CX□) and high-resolution transmission electron microscopy (HRTEM; Tecnai G^2F 20). The specific surface area, total pore volume, and average pore size were calculated using the surface area and pore-size analyzer (Quantachrome NOVA 2000e) at 77 K with samples degassed at 273 K under vacuum prior to each test. The adsorption spectra of TiO_2 catalysts were measured on a diffuse-reflectance UV−vis spectrometer (Shimadzu UV-3600) equipped with integrating spheres and using $BaSO_4$ as the reference. The thermal stability of the obtained samples was studied by thermogravimatric differential thermal analysis (TG-DTA; Rigaku PTC-10A). Each sample was treated under air and heated from room temperature to 800 °C at a rate of 10 °C/min.

2.3. Photocatalytic Activity Measurements. All photocatalytic experiments of gaseous toluene over mesoporous TiO_2 microspheres were performed in an XPA-2 photochemical reactor (Xujiang, Nanjing, China) equipped with a fixed-bed cylindrical quartz reactor of 1 L effective volume, which was horizontally located under irradiation of UV light accompanied by a water cooling system. A port at the top of the photoreactor was used for measuring the temperature and relative humidity and withdrawing toluene samples.

Approximately 0.5 g of the catalyst was dispersed in absolute ethanol in an ultrasonic field for 30 min. The resulting homogeneous suspension was uniformly loaded over the inside of the reactor as a thin film that exhibited good adhesion to the interior reactor. After the coated reactor was heated at 40 °C for 30 min to remove the dissolved ethanol, it was naturally cooled to room temperature for the next operation. Static vacuum gas distribution was adopted to obtain a certain amount of gaseous toluene in the coated reactor, and the detailed procedure can be seen in the Supporting Information. The toluene vapor was allowed to achieve gas−solid adsorption equilibrium with the coated catalysts for 2 h in the absence of UV illumination before photooxidation. Then, a 300 W UV mercury lamp with a peak wavelength of 365 nm was switched on, and the photocatalytic reaction was started. The vertical distance between the bottom of the reactor and the lamp was 30 cm.

The reacted gaseous samples were withdrawn at regular time intervals from 5 to 30 min by a 50 μL gastight pressure-locked precision analytical syringe (Gaoge, Shanghai, China) and measured with an Agilent 6820 gas chromatograph equipped with a flame ionization detector and an HP-5MS capillary column (0.25 mm i.d. × 30 m). The toluene conversion was calculated by the following equation:

$$\text{conversion}\ (\%) = \frac{C_t}{C_0} \times 100$$

where C_0 and C_t represent the toluene initial adsorption equilibrium concentration and reaction concentration, respectively. A blank experiment without catalyst under identical conditions was conducted to exclude the influence of photolysis on toluene conversion. For comparison, the photocatalytic activities of P_{25} were tested under the same conditions. All experiments were performed in triplicate. To test the repeatability, the whole experimental process (sampling and analysis) was conducted with P_{25} six times, and the resulting relative standard deviation was <3 %.

2.4. Reaction Intermediate Identification. Identification of the adsorbed intermediates was done by gas chromatography-mass spectrometry (GC−MS) after methanol extraction. The used catalyst dissolved in methanol (Fisher, HPLC grade) was subjected to ultrasound for 15 min. The suspension was centrifuged for 15 min at 3000 rpm, and the supernatant was concentrated by rotary evaporation. The condensed solution was directly analyzed by a GC−MS instrument (Aglient 6890) equipped with a HP-5MS capillary column and scanning from *m*/*z* 45 to 260. MS identification was based on the NIST 05 library with a fit higher than 90 %.

3. RESULTS AND DISCUSSION

3.1. Characterization of Mesoporous TiO_2 Microsphere Catalysts. An XRD technique was used to characterize the crystal structure and particle size of the samples (Figure 1). With an increase of the calcination temperature, the diffraction lines become sharper and narrower, indicating an increase of crystallinity with temperature (17). The diffraction peaks of the uncalcined samples, Ti100, Ti200, Ti300, Ti400, and Ti500 are indexed to the pure anatase phase. The phase transformation from anatase to rutile occurs at 600 °C, which is indicated by the results that Ti600 and Ti700 are anatase−rutile combinations. The average crystallite size of each sample was calculated by the Scherer equation (Table 1). These data reveal that a higher calcination temperature leads to bigger particles.

Figures 2 and 3 give the typical SEM and TEM images of uncalcined samples, Ti400, and Ti800 (SEM and TEM images of the other samples are shown in Figures S1 and S2 in the Supporting Information). As the SEM images indicate, all samples are microspheres with diameters of about 2 μm. With a higher calcination temperature, the surface of the microspheres becomes rougher, which is due to an increase of the crystalline size, and the results can be confirmed by XRD and TEM analysis. Though having been treated under various temperatures, there are no obvious changes in the sizes of the microspheres. The magnified SEM images indicate that those microspheres are constituted by small

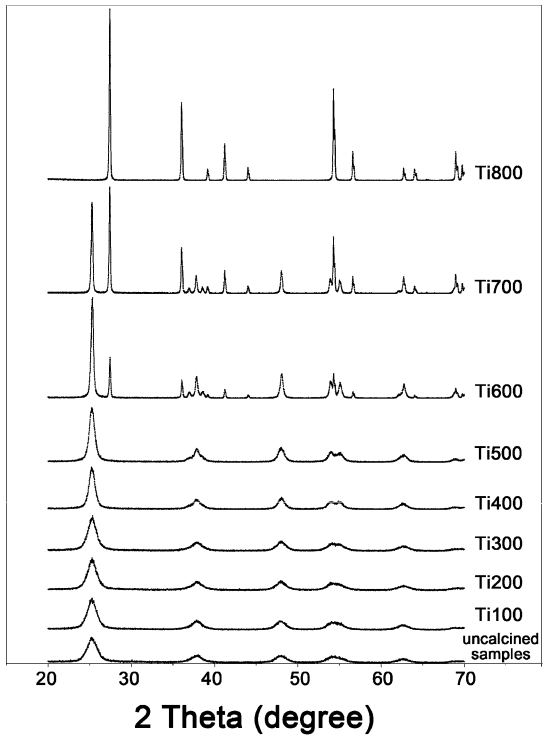

FIGURE 1. XRD patterns of all of the prepared samples calcined under different temperatures.

nanoparticles and there are internal pores in the spheres. TEM pictures show that these spheres are coarse and covered with agglomerates, which again confirms that the microspheres are constituted by particles. After calcination at higher temperatures over 700 °C, the mesopores collapsed, which is verified by the magnified SEM and TEM images of Ti700 and Ti800, and the results are consistent with N_2 adsorption−desorption data.

To investigate the pore structures and adsorption capacities of the mesoporous spherical TiO_2 catalysts, N_2 adsorption−desorption tests were performed and the experimental results are presented in Figure 4 and Table 1. The resulting isotherms of the above various catalysts show a typical IV pattern (IUPAC classification) with a hysteresis loop that is related to the capillary condensation associated with large mesopores (18), indicating the existence of mesopores. The formation of a mesoporous structure can be ascribed to aggregation of the TiO_2 particles. With an increase in the calcination temperature up to 400 °C, the hysteresis loops shift to a higher relative pressure (P/P_0) range and the areas of the hysteresis loops gradually become bigger. This indicates that the mean pore size and the pore volume increase with an increase in the calcination temperatures (19). When the uncalcined sample and Ti400 were compared, it was found that the average pore diameter enlarged from 2.70 to 11.56 nm, while the total pore volume increased from 0.22 to 0.33 mL/g, which is also confirmed by the FETEM images presented above. This can be attributed to two reasons. One was that the smaller pores endured much greater stress than the bigger pores, so the small pores collapsed first during calcination. The other was that the bigger crystallites could form bigger pores (11, 20). The mesostructure changes as a function of the calcination temperature. Higher calcination temperatures of 700 and 800 °C led to a drastic decrease in the surface area and a large increase in the particle size, indicating complete damage of the mesostructure, which was caused by material sintering (21). The crystal phase, crystalline particle size (nm), specific surface area (m^2/g), total pore volume (mL/g), average pore diameter (nm), band gap (eV), and reaction rate constant (min^{-1}) of all of the prepared samples together with P_{25} are summarized in Table 1.

The results through UV−vis spectra analysis show that the band-gap energy values of all TiO_2 samples calcined at 100, 200, 300, 400, 500, 600, 700, and 800 °C were in the range from 3.25 to 3.35 eV, as indicated in Figure S3 in the Supporting Information. The direct band-gap energies of P_{25} are 3.0 and 3.2 eV in the rutile and anatase phases, respectively. Herein, it is not surprising that the direct band-gap energies of the as-prepared powders are similar, although higher calcination treatments made the particles bigger and their thermal stabilities higher, as shown in Figures 1 (XRD pattern) and S4 in the Supporting Information (TG-DTA curves).

3.2. PCO for Toluene. Photocatalytic degradation of toluene involves different processes including adsorption−

Table 1. Structural Characteristics and Photocatalytic Constants of P_{25} and All of the Prepared Samples

sample	phase content[a]	crystalline size (nm)[b]	surface area (m^2/g)[c]	total pore volume (mL/g)[d]	average pore diameter (nm)[d]	band gap (eV)	average reaction rate constant (min^{-1})
P_{25}	A (80%) + R (20%)	21	58.8	0.15	1.88	3.2A/3.0R	0.0047
uncalcined	A	5.0	228.2	0.22	2.70	3.41	0.0048
Ti100	A	6.0	255.9	0.17	4.44	3.40	0.0057
Ti200	A	6.1	199.5	0.20	4.01	3.33	0.0070
Ti300	A	6.8	217.5	0.21	5.84	3.29	0.0068
Ti400	A	9.1	140.9	0.33	11.56	3.28	0.0077
Ti500	A	11.1	94.2	0.24	3.63	3.25	0.0073
Ti600	A (67%) + R (33%)	28.9A + 32.2R	25.9	0.22	6.30	3.45	0.0059
Ti700	A (41%) + R (59%)	57.2A + 36.2R	0			3.33	0.0028
Ti800	R	49.2	0			3.43	0.0010

[a] A and R denote the anatase and rutile phases, respectively. [b] The average crystalline size of TiO_2 was determined by XRD using the Scherer equation. [c] The BET surface area was determined by the multipoint BET method. [d] The pore volume and average pore size were calculated by the Barrett−Joyner−Halenda method (adsorption branch).

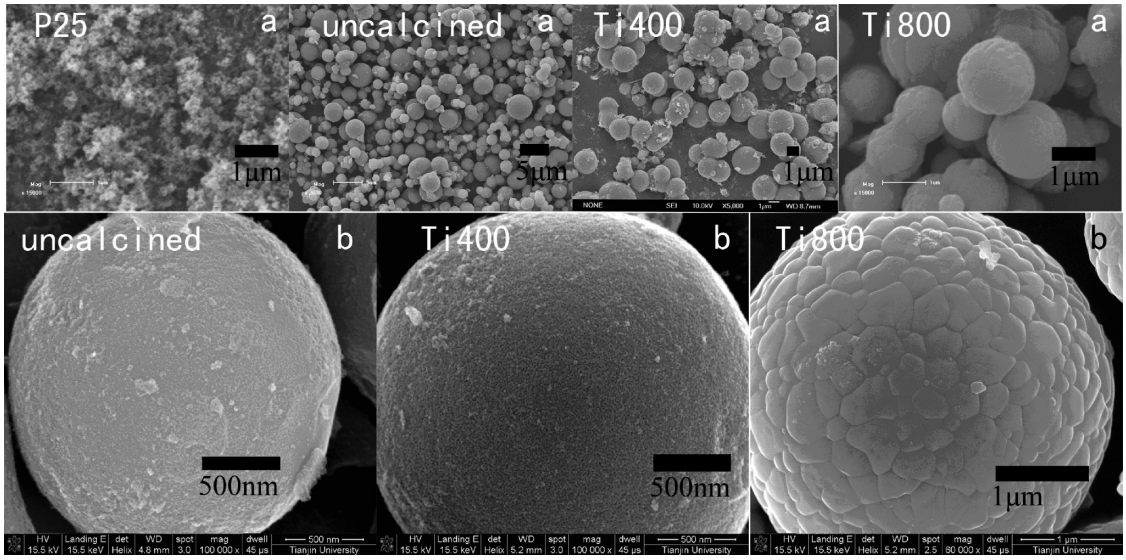

FIGURE 2. Typical SEM images of P_{25} and the prepared catalysts: (a) low magnification; (b) high magnification.

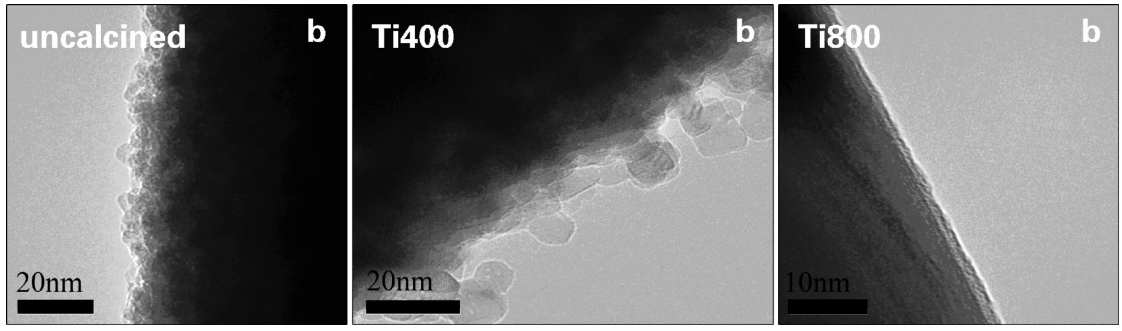

FIGURE 3. Typical magnified TEM images of the uncalcined TiO_2, Ti400, and Ti800.

desorption, electron−hole pair production and recombination, and chemical conversion. Every step has a relationship with characterization of the catalysts and shows obvious effects on the conversion rate. The reaction rate constant k was estimated by the pseudo-first-order reaction (19, 22). The kinetic equation is expressed as follows:

$$\ln \frac{c_0}{c_t} = kt$$

As our experiments indicated, direct photolysis has little effect on the toluene conversion. Figure 5A plots the toluene conversion as a function of the irradiation time; meanwhile, the reaction rate constants are compared in Figure 5B and Table 1. The results of the conversion rates revealed that the photocatalytic activity decreased in the order of Ti400 > Ti300 > Ti200 > Ti500 > Ti600 > Ti100 > P_{25} > uncalcined samples > Ti700 > Ti800, which is nearly consistent with the order of the reaction rate constants k. This reactivity order was constantly observed in almost all of our experiments. It is well-known that catalysts with bigger Brunauer−Emmett−Teller (BET) surfaces areas can supply relatively more active sites for adsorption and decomposition of the target reactants, exhibiting better catalytic properties. Mesoporous materials are of high surface area-to-volume ratios and lead to the confinement effect, which is based on a local increase in the partial pressure of reactants inside the nanometric channels of the mesostructure. They can supply relatively more active sites for adsorption and decomposition of the target reactants and allow light waves to penetrate deeply into the inside of TiO_2 by the pore channels, making it a much more efficient light harvester and resulting in an increase in the photoreaction rate (8, 14, 19, 23−26). The highest conversion of toluene was achieved by Ti400, with toluene conversion of 24.23% and an average reaction constant of 0.0077 min^{-1}, about 2-fold higher than that of P_{25}. The optimum photocatalytic performance observed was the synergetic effects of several factors, such as its anatase crystal phase, the increment of crystallinity induced by calcination, the high surface area-to-volume ratios, and high photon conversion efficiency (27). Ti600, though bearing relatively lower photon absorption ability, showed a superior photocatalytic performance, which may be due to the coexistence of the anatase and rutile phases. The anatase−rutile heterojunction structure can reduce the patterning dimension to the charge−separation distance and increase in the charge−separation efficiency, which is of importance in increasing the photocatalytic activity (28).

To further investigate the photocatalytic capability, the prolonged operation for P_{25} was conducted with an extra hour of illumination, and the conversion extent of P_{25} was

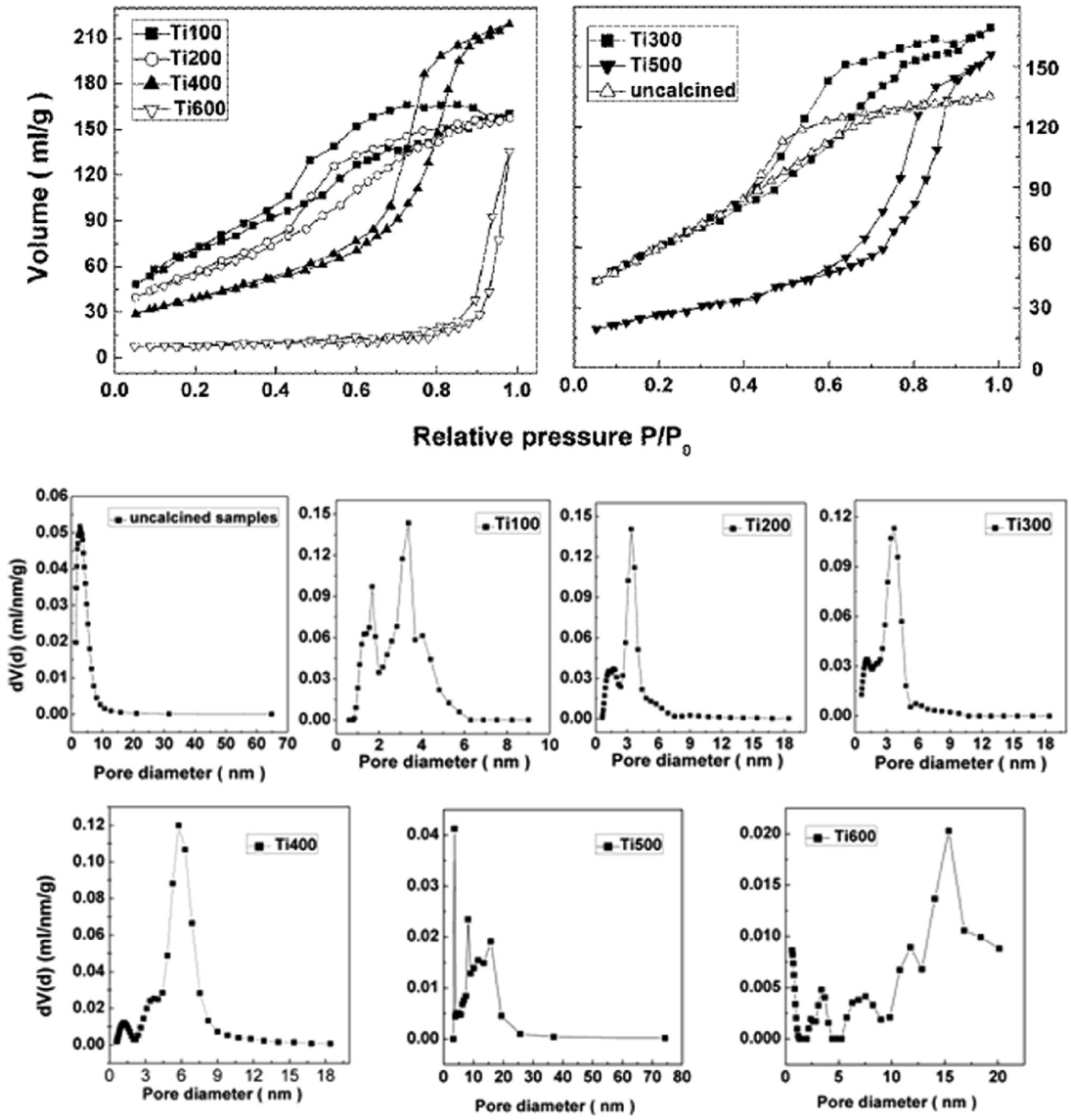

FIGURE 4. N_2 adsorption−desorption isotherms and pore size distribution of the prepared catalysts calcined from 100 to 600 °C with 100 °C intervals.

almost the same as that of Ti400. As discussed above, samples calcined at different temperatures ranging from 100 to 500 °C, including the noncalcined one, are all mesoporous materials and of the anatase phase; however, Ti400 exhibited a performance superior to the others. This again confirms that the process is affected by many factors. The anatase phase is reported to be more active than the rutile phase (29). Consequently, the photocatalytic activity of Ti800 is lower than that of other catalysts despite its other remarkable properties such as higher UV−vis adsorption ability, purity, and high thermal stability.

3.3. Intermediate Analysis. PCO reactions of VOCs proceed in a stepwise fashion. The intermediate is the reaction product of each step. The unintended intermediates can be toxic or irritating and may be less acceptable for human health and comfort than their precursors (5). These intermediates may also be strongly adsorbed on the surface of the TiO_2 catalyst and deteriorate its photoreactivity by blocking reaction sites (30). Therefore, it is necessary to identify the intermediates formed during the photocatalytic reaction.

GC−MS was employed to identify the adsorbed intermediates on the surface of the used catalysts. The possible intermediates in our reaction are listed in Table 2. Benzaldehyde, benzyl alcohol, cresol, hydroxybenzaldehyde, and benzoic acid were found in all used catalysts, which were also identified by several authors (12, 20, 31−35). The discrepancies of intermediates are found between the formulated catalysts and P_{25}. Trace amounts of complex hydroxylated intermediates (3,5-dihydroxytoluene and 2,5-dihydroxybenzaldehyde), benzene, and phenol were only formed during photooxidation of toluene using the synthesized catalysts. On the basis of the above observations, we propose a tentative degradation process (Figure 6A) for toluene photodegradation, and a representative GC−MS result is presented in Figure 6B. When TiO_2 is irradiated with photons higher than its band gap, electrons (e^-) and holes

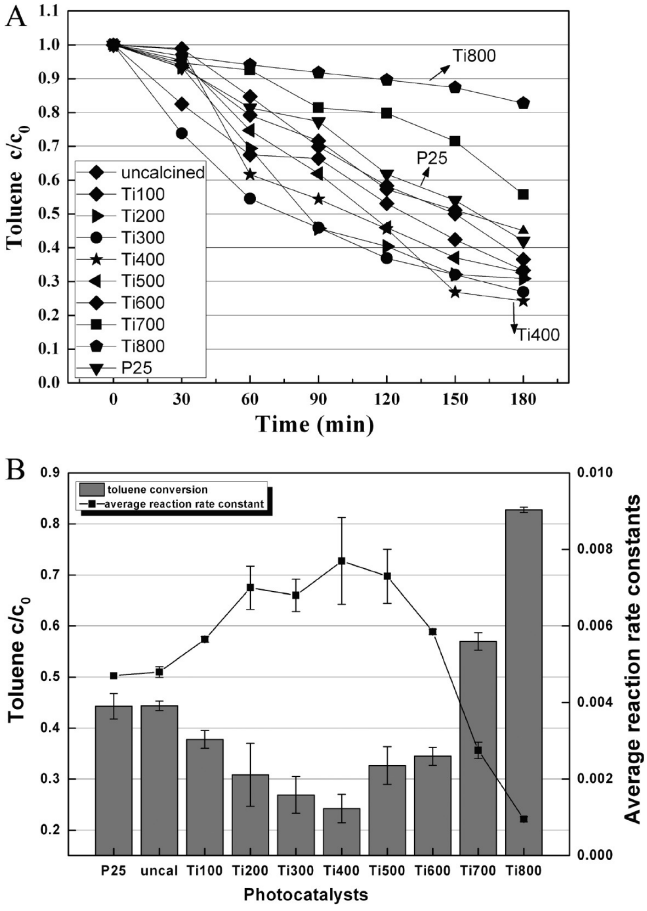

FIGURE 5. (A) Toluene conversion vs illumination time with P_{25} and the prepared samples. (B) Removal efficiency with various photocatalysts and their corresponding reaction rate constants.

Table 2. Possible Intermediates on the Used Catalysts

	compound name	retention time	*m/z*	entry number library (search index)
1	benzaldehyde	8.79	106.042	4937
2	phenol[a]	9.132	94.042	2533
3	benzyl alcohol	10.219	108.058	5223
4	2-hydroxybenzaldehyde	10.375	122.037	9583
5	2-methylphenol	10.48	108.058	5238
6	4-methylphenol	10.863	108.058	5230
7	benzoic acid	12.523	122.037	9580
8	benzene[a]	14.157	78.047	1000
9	4-hydroxybenzaldehyde[a]	14.454	122.037	10086
10	3-hydroxybenzaldehyde[a]	14. 464	122.037	9582
11	3,5-dihydroxytoluene[a,b]	14. 947	124.052	9588
12	2,5-dihydroxybenzaldehyde[a,b]	15.757	138.032	16662

[a] Intermediates detected on reacted synthesized samples only. [b] Intermediates first identified in the gas-phase toluene PCO.

(h^+) are generated. A portion of this photon-excited electron−hole pairs diffuses to the surface of the photocatalyts and reacts with H_2O to generate the surface hydroxyl groups (36), which then interact with the photogenerated holes h^+, producing hydroxyl radicals (31). These hydroxyl radicals can influence the first step of the reaction pathway in two different modes. In the first step, the hydroxyl radicals can directly add to the aromatic rings, yielding cresols, or extract a hydrogen atom from the side chain of toluene, the methyl groups of adsorbed toluene molecules, resulting in the formation of benzyl alcohol. The newly formed benzyl alcohol can be further oxidized to benzaldehyde and then

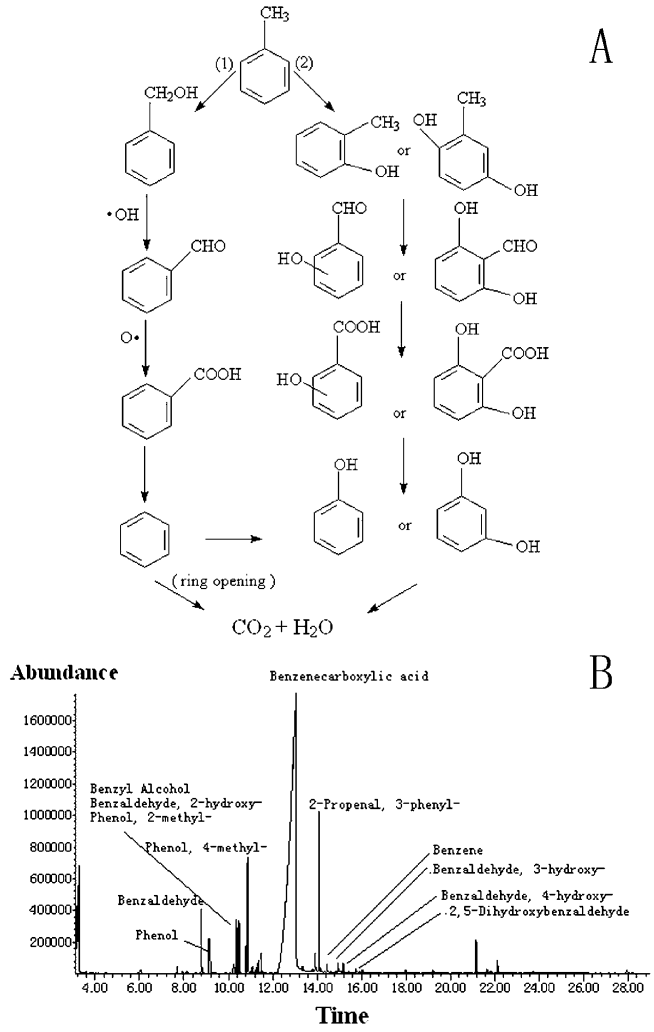

FIGURE 6. Proposed degradation process of toluene and a representative GC−MS result.

to benzoic acid. At the same time, a series of hydroxylations of the aromatic ring steps take place and lead to the generation of several hydroxylated intermediates (hydroxybenzaldehyde and their isomers) and even more complex identified compounds (3,5-dihydroxytoluene, 2,5-dihydroxybenzaldehyde, or their isomers). Traces of phenol are probably due to an attack of hydroxyl radicals to the benzene ring after photodecarboxylation of benzoic acid (35). When the benzyl ring is broken, the intermediates are oxidized into their complete oxidation products, CO_2 and H_2O.

During the whole reaction process, the surface hydroxyl groups, which can influence the process either by directly participating in the reaction mechanism or by affecting the adsorption of reactant molecules, can be restored by reactions involving adsorbed oxygen and water molecules. The above reaction pathway is consistent with the results described by other authors (12, 20, 31−34, 36) and the various intermediates identified in our tests. In parallel to that, compared with P_{25}, the complex hydroxyl derivatives (3,5-dihydroxytoluene and 2,5-dihydroxybenzaldehyde) formed using the synthesized catalysts are closely related to the hydrophilic properties of the mesoporous TiO_2, which concerns the density of the surface hydroxyl groups under UV

irradiation and leads to higher photocatalytic performances (37). During the process, water enhances the photocatalytic activity as long as it does not compete too strongly with the reactant for absorption, so abundant hydroxyl-radical population on the surface of the catalysts is beneficial for achieving superior photocatalytic performances (14). The higher photocatalytic performances of the various temperature-calcined catalysts are most probably with participation of these hydrogen-bonded hydroxyls. Meanwhile the complex intermediates may be related to its relatively higher decomposition behavior for the intermediates on the TiO_2 surface, which may enhance the photocatalytic performances by supplying more effective surface areas, so Ti400 achieved the highest conversion rate for toluene (38).

4. CONCLUSION

The effects of different calcination temperatures on the physiochemical and photocatalytic abilities of the synthesized mesoporous TiO_2 microspheres were investigated in this study. The textural, structural, and optical properties of the annealed catalysts were characterized by SEM, TEM, XRD, TG-DTA, UV−vis spectrophotometry, and N_2 adsorption−desorption measurements. It was found that calcination temperatures obviously influenced the surface morphology and photocatalytic activity of the mesoporous TiO_2 microspheres. As the results indicate, Ti100, Ti200, Ti300, Ti400, and Ti500 are all of the pure anatase phase with mesoporous structure, while at higher calcination temperatures of 600 and 700 °C, they changed to anatase−rutile combinations, and Ti800 was of the pure rutile phase. With increasing calcination temperatures, the specific surface areas and pore volumes decreased; however, the average crystallite size and pore size increased. In the PCO, Ti400 noticeably promoted the photocatalytic ability. The remarkably enhanced photoreactivity is attributed to the combined effects of its full crystallization, purity, thermal stability, better optical absorption properties, and mesoporous structure, which plays a leading role in increasing the conversion rate. Besides (or in addition to) the previously reported compounds, small amounts of complex hydroxylated intermediates (3,5-dihydroxytoluene and 2,5-dihydroxybenzaldehyde) were also discovered using the synthesized TiO_2 as catalysts by GC−MS analysis. The degradation pathway was proposed in this study, indicating the formed complex hydroxyl derivatives. However, further studies are required to ascertain the role of hydroxyl groups in the photooxidation of organic species on the surface of the catalysts.

Acknowledgment. This research was supported by the 2008 National Science Foundation of China (Grant 20877042) and the China−U.S. Center for Environmental Remediation and Sustainable Development.

Supporting Information Available: Annotations I−IV, SEM and TEM images, UV−vis spectra, and TG-DTA curves. This material is available free of charge via the Internet at http://pubs.acs.org.

REFERENCES AND NOTES

(1) Phan, T. D. N.; Song, M. B.; Shin, E. *J. Hazard. Mater.* **2009**, *167*, 75.
(2) Durme, J. V.; Dewulf, J.; Sysmans, W.; Leys, C.; Langenhove, H. V. *Chemosphere* **2007**, *68*, 1821.
(3) Yu, H.; Lee, S. C.; Yu, J.; Ao, C. H. *J. Mol. Catal. A: Chem.* **2006**, *246*, 206.
(4) Wang, J. H.; Ray, M. B. *Sep. Purif. Technol.* **2000**, *19*, 11.
(5) Mo, J. H.; Zhang, Y. P.; Xu, Q. J.; Lamson, J. J.; Zhao, R. Y. *Atmos. Environ.* **2009**, *43*, 2229.
(6) Maira, A. J.; Yeung, K. L.; Soria, J.; Coronado, J. M.; Belver, C.; Lee, C. Y.; Augugliaro, V. *Appl. Catal., B* **2001**, *29*, 327.
(7) Zhao, J.; Yang, X. D. *Build. Environ.* **2003**, *38*, 645.
(8) Maira, A. J.; Yeung, K. L.; Lee, C. Y.; Yue, P. L.; Chan, C. K. *J. Catal.* **2000**, *192*, 185.
(9) Anpo, M.; Takeuchi, M. *J. Catal.* **2003**, *216*, 505.
(10) Li, F. B.; Li, X. Z.; Ao, C. H.; Lee, S. C.; Hou, M. F. *Chemosphere* **2005**, *59*, 787.
(11) Yu, J. G.; Zhou, M. H.; Cheng, B.; Yu, H. G.; Zhao, X. J. *J. Mol. Catal. A: Chem.* **2005**, *227*, 75.
(12) Sleiman, M.; Conchon, P.; Ferronato, C.; Chovelon, J. *Appl. Catal., B* **2009**, *86*, 159.
(13) Hernández-Alonso, M.; Hungría, A. B.; Martínez-Arias, A.; Fernández-García, M.; Coronado, J. M.; Conesa, J. C.; Soria, J. *Appl. Catal., B* **2004**, *50*, 167.
(14) Bosc, F.; Edwards, D.; Keller, N.; Keller, V.; Ayral, A. *Thin Solid Films* **2006**, *495*, 272.
(15) Pavasupree, S.; Ngamsinlapasathian, S.; Nakajima, M.; Suzuki, Y.; Yoshikawa, S. *J. Photochem. Photobiol. A* **2006**, *184*, 163.
(16) Guo, C. S.; Ge, M.; Liu, L.; Gao, G. D.; Feng, Y. C.; Wang, Y. Q. *Environ. Sci. Technol.* **2010**, *44*, 419.
(17) Wang, Y. G.; Yuan, X. H.; Liu, X. H.; Ren, J. W.; Tong, W. Y.; Wang, Y. Q.; Lu, G. Z. *Solid State Sci.* **2008**, *10*, 1117.
(18) Ismail, A. A.; Bahnemann, D. W.; Bannat, I.; Wark, M. *J. Phys. Chem. C* **2009**, *113*, 7429.
(19) Zhou, M. H.; Yu, J. G.; Liu, S. W.; Zhai, P. C.; Huang, B. B. *Appl. Catal., B* **2009**, *89*, 160.
(20) Cao, L. X.; Suib, S. L.; Obee, T. N.; Hay, S. O.; Freihaut, J. D. *J. Catal.* **2000**, *196*, 253.
(21) Barraud, E.; Bosc, F.; Edwards, D.; Kelle, N.; Keller, V. *J. Catal.* **2005**, *235*, 318.
(22) Dong, F.; Wang, H. Q.; Wu, Z. B. *J. Phys. Chem. C* **2009**, *113*, 16717.
(23) Liu, Y.; Li, Y.; Wang, Y. T.; Xie, L.; Zheng, J.; Li, X. G. *J. Hazard. Mater.* **2008**, *150*, 153.
(24) Fresno, F.; Coronado, J. M.; Tudela, D.; Soria, J. *Appl. Catal., B* **2005**, *55*, 159.
(25) Kar, A.; Smith, Y.; Subramanian, V. *Environ. Sci. Technol.* **2009**, *43*, 3260.
(26) Wang, X. C.; Yu, J. C.; Ho, C.; Hou, Y. D.; Fu, X. Z. *Langmuir* **2005**, *21*, 2552.
(27) Lin, H.; Huang, C. P.; Li, W.; Ni, C.; Shah, S. I.; Tseng, Y. *Appl. Catal., B* **2006**, *68*, 1.
(28) Kawahara, T.; Konishi, Y.; Tada, H.; Tohge, N.; Nishii, J.; Ito, S. *Angew. Chem., Int. Ed.* **2002**, *41*, 2811.
(29) Bacsa, R. R.; Kiwi, J. *Appl. Catal., B* **1998**, *16*, 19.
(30) Jeong, J.; Sekiguchi, K.; Sakamoto, K. *Chemosphere* **2004**, *57*, 663.
(31) Martra, G.; Coluccia, S.; Marchese, L.; Augugliaro, V.; Loddo, V.; Palmisano, L.; Schiavello, M. *Catal. Today* **1999**, *53*, 695.
(32) Maira, A. J.; Coronado, J. M.; Augugliaro, V.; Yeung, K. L.; Conesa, J. C.; Soria, J. *J. Catal.* **2001**, *202*, 413.
(33) Blount, M. C.; Falconer, J. L. *Appl. Catal., B* **2002**, *39*, 39.
(34) Coronado, J. M.; Kataoka, S.; Tejedor-Tejedor, I.; Anderson, M. A. *J. Catal.* **2003**, *219*, 219.
(35) Augugliaro, V.; Coluccia, S.; Loddo, V.; Marchese, L.; Martra, G.; Palmisano, L.; Schiavello, M. *Appl. Catal., B* **1999**, *20*, 15.
(36) Einaga, H.; Futamura, S.; Ibusuki, T. *Appl. Catal., B* **2002**, *38*, 215.
(37) Ramirez, A. M.; Demeestere, K.; Belie, N. D.; Mantyla, T.; Levanen, E. *Build. Environ.* **2010**, *45*, 832.
(38) Einaga, H.; Ibusuki, T.; Futamura, S. *Environ. Sci. Technol.* **2004**, *38*, 285.

AM100620F